PCCP

Accepted Manuscript




ROYAL SOCIETY OF CHEMISTRY

www.rsc.org/pccp

# Evolution of Oxidation Dynamics of Histidine: Non-Reactivity in the Gas Phase, Peroxides in Hydrated Clusters, and pH Dependence in Solution

Fangwei Liu, Wenchao Lu, Yigang Fang,[a] Jianbo Liu*

Department of Chemistry and Biochemistry

Queens College and the Graduate Center of the City University of New York

65-30 Kissena Blvd., Queens, New York 11367, USA

* Author to whom correspondence should be addressed. Electronic mail: jianbo.liu@qc.cuny.edu.

[a] Present address: Chemical Sciences Division, Lawrence Berkeley National Laboratory, Berkeley, CA 94720

**Abstract**

Oxidation of histidine by $^1O_2$ is an important process associated with oxidative damage to proteins during aging, diseases and photodynamic therapy of tumors and jaundice, and photochemical transformations of biological species in the troposphere. However, the oxidation mechanisms and products of histidine differ dramatically in these related environments which range from the gas phase through aerosols to aqueous solution. Herein we report a parallel gas- and solution-phase study on the $^1O_2$ oxidation of histidine, aimed at evaluating the evolution of histidine oxidation pathways in different media and at different ionization states. We first investigated the oxidation of protonated and deprotonated histidine ions and the same systems hydrated with explicit water molecules in the gas phase, using guided-ion-beam-scattering mass spectrometry. Reaction coordinates and potential energy surfaces for these systems were established on the basis of density functional theory calculations, Rice-Ramsperger-Kassel-Marcus modeling and direct dynamics simulations. Subsequently we tracked the oxidation process of histidine in aqueous solution under different pH conditions, using on-line UV-Vis spectroscopy and electrospray mass spectrometry monitoring systems. The results show that two different routes contribute to the oxidation of histidine depending on its ionization states. In each mechanism hydration is essential to suppressing the otherwise predominant dissociation of reaction intermediates back to reactants. The oxidation of deprotonated histidine in the gas phase involves the formation of 2,4-endoperoxide and 2-hydroperoxide of imidazole. These intermediates evolve to hydrated imidazolone in solution, and the latter either undergoes ring-closure to 6α-hydoxy-2-oxo-octahydro-pyrrolo[2,3-d]imidazole-5-carboxylate or cross-links with another histidine to dimeric product. In contrast, the oxidation of protonated histidine is mediated by 2,5-endoperoxide and 5-hydroperoxide, which convert to stable hydrated imidazolone end-product in solution. The contrasting mechanisms and reaction efficiencies of protonated *vs.* deprotonated histidine, which lead to pH dependence in the photooxidation of histidine, are interpreted in terms of the chemistry of imidazole with $^1O_2$. The biological implications of the results are also discussed.

## 1 Introduction

Histidine (His), with an imidazole side chain, is an essential proteinogenic amino acid (AA), and is frequently contained at the active sites of enzymes. Examples that demonstrate the importance of His are its capability of oxygen binding in myoglobin[1] and hemoglobin,[2] its involvement in catalyzing reversible oxidation of hydrogen in hydrogenases,[3] and its cooperative role in catalytic triads such as Ser-His-Asp in chymotrypsin.[4] His is also one of the most susceptible residues toward singlet $O_2[a^1\Delta_g]$-mediated photooxidation,[5, 6] where the electronically excited $^1O_2$ is generated via energy transfer from the triplet excited state of an endogenous or exogenous sensitizer to $^3O_2$ (type II photosensitization).[7] The photooxidation of His results in inactivation of His-containing enzymes[8] and protein cross-linking and aggregation.[9] This photodynamic action, besides its damaging interaction with biomolecules, finds applications in phagocytosis and photodynamic therapy of cancer and newborn jaundice.[10, 11] In addition to biochemical milieu, His is ubiquitous in tropospheric particles and depositions,[12] and undergoes transformations due to photochemically formed reactive oxygen species.[13, 14] It was reported that oxidation by $^1O_2$ accounts for half of the loss of His in the troposphere in California′s Central valley.[14]

The photooxidation of His shows complex pathways with yet poorly characterized products. We have summarized literature proposed primary oxidation pathways of His in Fig. S1.[5, 15-18] One unique feature of His photooxidation is its strong pH dependence. The oxidation does not take place appreciably below pH 6, starts to increase above that and levels off at pH > 8.[19-23] The pH dependence resembles the titration curve of imidazole, emphasizing the influences of imidazole ionization states. Biological implications of this pH dependence are obvious considering the fact that His (with carboxyl p$K_a$ of 1.70, amino p$K_a$ of 9.12, and imidazole p$K_a$ of 6.04) is the third strongest basic AA and the third strongest acidic AA[24], and is the only residue that may undergo both protonation and deprotonation in physiological pH range. Besides solution pH, the photooxidation of His is influenced by varying sensitizers, illumination time and solvents,[18] and interference drawn from free radical-mediated (type I)[11] photosensitization. As a result, despite decades of experimental studies devoted to the elucidation of His

photooxidation, quantitative information is limited concerning major intermediates, pathways and product structures and their biological relevance. On the other hand, theoretical study on the photooxidation of His has emerged only recently.[25]

Compared to the photooxidation study of His and other AAs in solution, much less has been done for these systems in the gas phase. However, gas-phase experiments are no less important considering their capability in providing detailed pictures of reactions and their environmental and atmospheric implications. We have investigated the reactions of $^1O_2$ with AAs and model dipeptides in the gas phase[26-31] using ion-beam-scattering methods[32] and electrospray-ionization mass spectrometry (ESI MS).[33] Gas-phase experiments can distinguish the intrinsic reactivities of AAs from solvent and counter-ion effects, providing a basis for understanding their photooxidation mechanisms. Note that the presence of hydrogen-bonded water molecules is critical for molecule dynamics,[34] and we have taken this into account in gas-phase experiments and obtained encouraging results. Taking the $^1O_2$ oxidation of cysteine (Cys) as an example,[28, 30, 35] the oxidation of bare Cys (either protonated or deprotonated) dumped reaction exoergicity into products and caused fragmentation of the Cys moiety. Nevertheless, the addition of water ligands to the system suppressed product dissociation and intrinsically influenced oxidation pathways. Pathways that are normally not feasible in the gas phase become so in Cys-water clusters.

Experiments on gaseous hydrated clusters not only simplify data interpretations, but provide a microscopic view of more biologically relevant dynamics than gas-phase isolated molecules. On the other hand, gas-phase experiments in explicit ″microsolution″ still differ from those in an aqueous continuum. For example, the low number density of molecules in the gas phase may prohibit secondary reactions and further conversion of intermediates and primary products. Therefore it is not surprising if the reaction products of gaseous hydrated clusters do not exactly match those in bulk solution. Questions then arise: to what extent the intermediates and products observed in the gas phase resemble or relate to the products in aqueous solution, and how to extrapolate gas-phase reaction profiles to solution-phase reactions. More to the point, how reaction dynamics and products evolve from isolated gas-phase species

to different hydrated media.

With the above motivations and questions in mind, we have carried out systematic investigations on the $^1O_2$ oxidation of His at different ionization states and in different media ranging from isolation in the gas-phase, through clustering with an explicit number of water molecules, to bulk aqueous solution. Ion-molecule scattering experiment was carried out for $^1O_2$ with His at various gas-phase states (protonated *vs.* deprotonated, and dry *vs.* mono- and dihydrated) using a guided-ion-beam tandem mass spectrometer coupled with an ESI source.[26, 27] Gas-phase results are interpreted with the aid of density functional theory (DFT) electronic structure calculations, Rice-Ramsperger-Kassel-Marcus (RRKM)[36] kinetics modeling and direct dynamics trajectory simulations.[37] Mass spectrometry and spectroscopic data were then obtained in real-time for the oxidation of His in aqueous solution under different pH conditions. Parallel gas- and solution-phase experiments undertaken in a synergistic way have led to a sound understanding of the chemistry underlying the oxidation of such a biologically important AA.

## 2 Experimental and Computational Details

### 2.1 $^1O_2$ generation and detection

$^1O_2$ was generated based on the reaction of $H_2O_2 + Cl_2 + 2KOH \rightarrow O_2$(~85% $X^3\Sigma_g^-$ and ~15% $a^1\Delta_g$) + $2KCl + 2H_2O$.[27, 29, 38] As shown in Fig. 1, 13 mL of 8 M KOH was added to 20 mL of 35 w.t.% aqueous $H_2O_2$ in a sparger (**1**) held at -19 °C, and the resulting mixture was degassed. 2.6 sccm of $Cl_2$ (≥ 99.5%, Sigma-Aldrich) was mixed with 50 sccm of He and bubbled through the $H_2O_2$/KOH slush. The reaction converted $Cl_2$ completely to ground-state and excited $O_2$. Resulting gas products passed through a cold trap (**2**, kept at -70°C) to remove water vapor. Only $^3O_2$, $^1O_2$ and He remained in the downstream gas. The concentration of $^1O_2$ in the gas was determined by measuring $^1O_2$ emission ($a^1\Delta_g \rightarrow X^3\Sigma_g^-$, $\nu = 0 - 0$)[39] at 1270 nm in an optical emission cell (**3**). Emission from the cell was collected by a plano-convex BK7 lens ($f$ = 30 mm), passed through an optical chopper (SRS model SR540) and a 5-nm bandwidth interference filter centered at 1270 nm, and focused by another plano-convex BK7 lens ($f$ = 50mm) into a thermoelectrically cooled InGaAs detector (**4,** Newport 71887) coupled with a lock-in amplifier (Stanford

Research Systems SR830). The amplifier output was converted to absolute $^1O_2$ concentration based on a previous calibration.[29] To reduce the residence time of $^1O_2$ and therefore minimize its wall quenching and self-quenching, the whole generator was continuously evacuated to 25 τ through a pressure relay (**6**). $^1O_2$ (mixed with $^3O_2$ and He) was either introduced into the scattering cell of a guided-ion-beam mass spectrometer for gas-phase ion-molecule reactions, or bubbled into an aqueous reaction vessel (**5**).

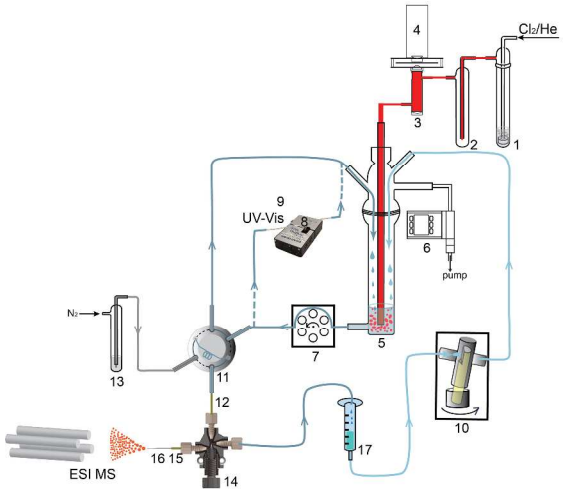


**Fig. 1** $^1O_2$ generation, detection and on-line reaction monitoring system.

### 2.2 Ion-molecule scattering experiment

Gas-phase reactions were performed using a home-made guided-ion-beam tandem mass spectrometer, which has been described previously along with operation, calibration and data analysis procedures.[26, 29] Protonated $HisH^+$ was prepared in methanol-water (1:1 vol. ratio) containing 0.5 mM His (≥99%, Sigma-Aldrich) and an equimolar amount of HCl, and deprotonated $[His-H]^-$ was prepared in methanol-water (2:1) containing 0.5 mM His and NaOH. Sample solution was sprayed into an ambient atmosphere through an electrospray needle at a rate of 0.04 $mL \cdot h^{-1}$. The ESI needle was held at 2.3 and -2.2 kV for producing positively and negatively charged species, respectively. Charged droplets entered the source chamber of the mass spectrometer through a desolvation capillary. The capillary was heated to 170 °C for generating dry ions, 122 °C for monohydrated ions, and 118 °C for dihydrated ions. Ions were transported into a hexapole ion guide at a pressure of 28 mTorr, and underwent collisional focusing and

cooling to ~310 K. Ions subsequently passed into a conventional mass-selecting quadrupole for selection of specific reactant ions. Reactant ions were collected and focused into an octopole ion guide, which trapped ions in radial direction. DC bias voltage was applied to the octopole ion guide with variable amplitude, to determine the initial kinetic energy of selected ions using retarding potential analysis.[40] The DC bias voltage also allowed control of the kinetic energy ($E_{lab}$) of ions in the laboratory frame, thereby setting the collision energy ($E_{col}$) between ions and reactant gas molecules in the center-of-mass frame, *i.e.*, $E_{col} = E_{Lab} \times m_{neutral} /(m_{ion} + m_{neutral})$, where $m_{neutral}$ and $m_{ion}$ are the masses of neutral and ionic reactants, respectively. The octopole passes through a scattering cell containing $^1O_2$. Product ions resulting from reactions with $^1O_2$ and unreacted primary ions were collected by the octopole, passed into a second quadrupole for mass analysis and counted. Reaction cross sections at different $E_{col}$ were calculated from the ratio of reactant and product ion intensities, the pressure of $^1O_2$ in the scattering cell ( = the total gas pressure in the cell measured by a Baratron capacitance manometer × the fractional abundance of $^1O_2$ determined from $^1O_2$ emission), and the effective cell length. The scattering cell pressure was set at 0.28 mTorr containing 5% of $O_2$ and 95% of He. Under these conditions, His ions underwent at most a single collision with $O_2$. His ions also collided with He, but heavy ion-light neutral combination made these collisions insignificant at low $E_{col}$.

### 2.3 On-Line monitoring of aqueous reactions

Over the course of aqueous reaction, UV-Vis absorption and/or ESI mass spectra of the reaction solution were recorded continuously. As illustrated in Fig. 1, a peristaltic pump (**7**) circulated the aqueous solution (containing 0.5 mM His at different pH) in **5** through a quartz flow cell (**8**) of 1-cm optical path length. UV-Vis absorption of the solution was recorded by an Ocean Optics USB4000 diode array spectrometer (**9**) at 30-sec intervals. As explained in Section 2.1, the whole system was pumped down to 25 τ (slightly above water vapor pressure), which resulted in evaporation of a significant amount of water from **5**. To compensate the water loss in **5**, extra water was replenished through an Ismatec Reglo-CPF rotary piston pump (**10**) at a precisely controlled flow rate.

For ESI MS monitoring, the first quadrupole of our tandem mass spectrometer was rendered to an rf-only ion guide, and ions were mass-scanned by the second quadrupole. To the best of our knowledge, most of the on-line ESI MS monitoring methods[41-47] were reported for reactions running at a pressure near atmospheric or higher, where reaction solutions can be transported to ESI by gravity or positive gas pressure. Our system, on the other hand, was operating at 25 τ. To transport the reaction solution from low pressure to open-air ESI, we used a sampling loop (1 mL size) coupled to a 2-position switching valve (**11**). For each measurement, the valve was placed in load position for 3 seconds to fill the loop from **5**, and then switched to injection. The water from a reservoir (**13**) swept the sample in the loop to ESI through a 0.0625″ o.d. × 0.04″ i.d. PEEK tubing (**12**) under 4-psi gauge pressure of $N_2$. To reduce the sample transfer time (< 30 sec), we adopted Cooks and coworkers' method[47] by adding an adjustable micro-splitter (**14**) to sample line. The split stream (0.04 mL·h$^{-1}$) from **14** was directed to the ESI needle (**16**) through a 0.0625 ″ o.d. × 0.007″ i.d. × 1″ length PEEK tubing (**15**). To avoid discharge in negative ESI of water solution,[48] methanol (0.04 mL·h$^{-1}$) was added to the split stream through a microtee (not shown in Fig. 1) between **14** and **15**. The waste stream (11.4 mL·h$^{-1}$) from **14** was collected in a container (**17**), and returned to **5** through **10**. As in the UV-Vis measurement, extra water was added to **5** for compensating the evaporation loss.

To check the reactivity of His toward $^3O_2$/He in different systems, control experiments were performed under the same conditions as those performed with $^1O_2$ except that $Cl_2$ used for the $^1O_2$ chemical generator was replaced by $O_2$ gas at the same flow rate.

**2.4 Electronic structure calculations, RRKM modeling and direct dynamics simulations**

Geometries of reactants, intermediates, transition states (TSs) and products were optimized using Gaussian 09,[49] at B3LYP and MP2 levels of theory with 6-31+G(d) and 6-311++G(d,p) basis sets. Conformation searching was conducted for all reactant ions, and their most stable conformations were used as starting structures in reaction coordinates, RRKM modeling and trajectories. All the TSs were verified as first-order saddle points, and the vibrational mode with an imaginary frequency corresponds to

the associated reaction pathway. DFT-calculated vibrational frequencies and zero-point energies (ZPE) were scaled by a factor of 0.952 and 0.977; and MP2-calculated frequencies and ZPE were scaled by a factor of 0.945 and 0.970, respectively.[50] All energies in this work were calculated with thermal corrections to 298 K (including ZPE). RRKM rates and density of states (DOS) were calculated with the program of Zhu and Hase,[51] using direct state count algorithm and scaled DFT frequencies and energetics.

Direct dynamics simulations for the reactions of $^1O_2$ with $HisH^+(H_2O)_{0,1}$ and $[His\text{-}H]^-(H_2O)_{0,1}$ were carried out at $E_{col}$ = 0.1 eV using the Venus software[52] interfaced with Gaussian 09. One hundred trajectories were accumulated for each system. Considering the accuracy and the computational cost, the B3LYP/6-31G(d) level of theory was chosen for trajectory integration. The initial separation between reactant ion and $^1O_2$ was set at 8.0 Å (where the attractive potential between reactants is less than a few meV), with a collision impact parameter of 0.1 Å. The vibrational and rotational temperatures of all reactants were set at 300 K, which were chosen to mimic our ion-beam experiments. Quasi-classical Boltzmann sampling[53] was used to select their vibrational and rotational energies.

Hessian-based predictor-corrector algorithm[54] was used for numerical integration of the classical equations of motion, with Hessian matrix updated every five steps. A step size of 0.25 $amu^{1/2}$Bohr (corresponding to a step size of ~0.5 fsec in trajectory time) was used for trajectories. The initial guess of molecular orbital for each DFT calculation was obtained from previous step, and the total energy of the system was checked during the simulation to ensure the energy was conserved to better than $10^{-4}$ Hartree. The SCF = XQC option was adopted for the trajectory integration so that a quadratically convergent SCF method was used in case the conventional first-order SCF algorithm failed to converge within allotted cycles. Most trajectories were terminated after 6 psec or when the product separation exceeded 8.1 Å. gOpenMol[55] was used for trajectory visualization. Analysis of individual trajectories and statistical analysis of the trajectory ensemble were done with programs written for this purpose.

## 3 Results and discussion

### 3.1 Protonation, deprotonation and hydration of His in the gas phase

**3.1.1 $HisH^+(H_2O)_{n=0-2}$.** Reactant ions of His were generated by ESI in our gas-phase experiments. One issue for interpretation of His ion chemistry is that His ions exist in various conformations resulting from the flexibility of their structures. His has two tautomers, *i.e.*, the τ tautomer with an H bound to $N^{\tau}$ and the π tautomer with an H to $N^{\pi}$ (see the numbering scheme of the imidazole ring in Fig. 2). Accordingly, His may adopt three different structures upon protonation. We included imidazole tautomeric state and His protonation site in the notations of $HisH^+$ structures, *i.e.*, $His^{\tau}H_{am}^+$ and $His^{\pi}H_{am}^+$ correspond to protonation at the α-amino group of the τ and π tautomers, respectively; and $HisH_{im}^+$ due to protonation of either imidazole N atom. A grid search method was used to find global minima in the conformation landscapes of $His^{\tau}H_{am}^+$, $His^{\pi}H_{am}^+$ and $HisH_{im}^+$. Each of the torsion angles of His backbone was rotated systematically through 360° at 60°-increment to generate trial staggered conformations for $His^{\tau}H_{am}^+$, $His^{\pi}H_{am}^+$ and $HisH_{im}^+$. Every conformation so generated was subjected to optimization at B3LYP/6-31+G(d) to derive associated local minimum conformation. These conformations were then re-optimized at B3LYP/6-311++G(d,p) and MP2/6-311++G(d,p). A total of 29 conformers were found for $HisH^+$ as summarized in Fig. S2. Each conformer has a number suffix to denote the ordering of stability within its structure category. We have calculated relative energies of these conformers at pressures of one atmosphere *vs.* ~mTorr, with no obvious changes. Our conformation search reproduced the stable $HisH^+$ conformers/tautomers reported by others,[24, 56-64] and identified many new ones.

In solution the α-amino of His is more basic than the imidazole ring, but in the gas phase the imidazole ring becomes slightly more favorable for protonation. In Fig. 2 we present the two lowest-energy conformers for each of $HisH_{im}^+$ (imidazole protonated) and $His^{\tau}H_{am}^+$ (α-$NH_2$ protonated). $HisH_{im}^+$_1 and $His^{\tau}H_{am}^+$_2, and $HisH_{im}^+$_2 and $His^{\tau}H_{am}^+$_1, are prototropic tautomers. $HisH_{im}^+$_1 is the lowest-lying conformation at both B3LYP and MP2 levels, and $His^{\tau}H_{am}^+$_2 becomes the second lowest at MP2/6-311+G(d,p) with an energy only 0.02 eV above $HisH_{im}^+$_1. The subtle energy difference between $HisH_{im}^+$_1 and $His^{\tau}H_{am}^+$_2 implies that His bears two nearly equal protonation sites at imidazole $N^{\pi}$ and

backbone $N^{\alpha}$, and the proton shuttles between $N^{\pi}$ and $N^{\alpha}$.[56, 61] Based on DFT energies, $HisH_{im}^{+}$_1 and 2 dominate the gas-phase structure of $HisH^{+}$ at 298 K with percentage shares of 42 and 27, respectively. This predication is consistent with the infrared multiple photon dissociation spectroscopy which identified $HisH_{im}^{+}$ as the dominating structure.[61] However, due to the "mobile" proton along $N^{\pi}\cdots H\cdots N^{\alpha}$, $His^{\tau}H_{am}^{+}$_2 would be expected to emerge during reactions. We have therefore included both $HisH_{im}^{+}$ and $His^{\tau}H_{am}^{+}$ structures in the DFT exploration of hydrate structures and reaction coordinate.

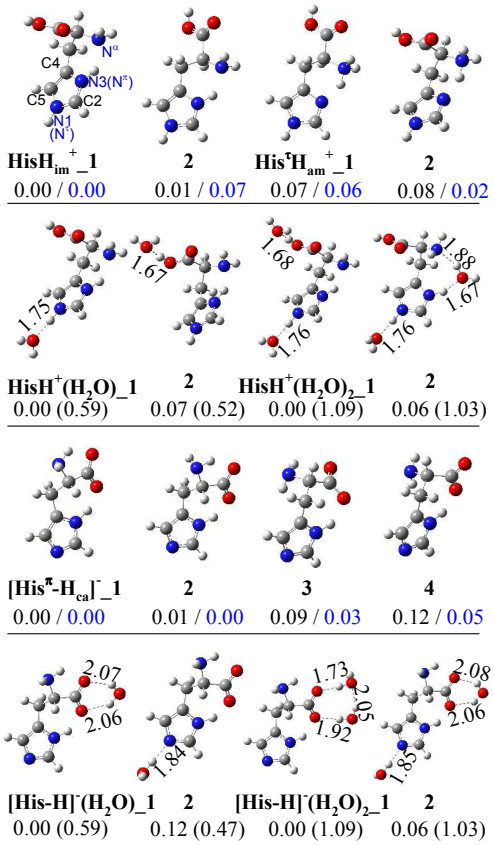


**Fig. 2** Low-lying conformers/tautomers of dry and hydrated $HisH^{+}$ and $[His\text{-}H]^{-}$. Hydrogen bonds (---) between His and water(s) are shown in Å. For $HisH^{+}$ and $[His\text{-}H]^{-}$, relative energies (eV) shown before slashes are derived from B3LYP/6-311++G(d,p), followed by values (in blue) from MP2/6-311++G(d,p). For $HisH^{+}(H_2O)_{1,2}$ and $[His\text{-}H]^{-}(H_2O)_{1,2}$, only relative energies at B3LYP/6-311++G(d,p) are indicated, along with hydration energies presented in parentheses.

Similar as the calculation of hydrated neutral His,[65] trial geometries of $HisH^{+}(H_2O)$ were obtained by

adding a water to all possible hydration sites on $HisH_{im}^+$_1 and $His^{\tau}H_{am}^+$_2, and then optimized at B3LYP/6-311++G(d,p). Seven stable conformations of monohydrate were found as shown in Fig. S3, and the most stable two (with populations of 94% and 5.6%, respectively) are included in Fig. 2. Hydration energy was calculated using $E_{hydration}$= $E$(bare ion) + $nE(H_2O)$ - $E$(cluster), where $E$(bare ion), $E(H_2O)$ and $E$(cluster) are the DFT energies of bare ion, water and the hydrate of the same ion conformation, respectively. The carboxyl, ammonium, amino and imino groups each offers a binding site for water with $E_{hydration}$ of 0.52, 0.40, 0.34, and 0.59(-$N^{\tau}$H)/0.38 eV(-$N^{\pi}$H), respectively.

Structures of $HisH^+(H_2O)_2$ (see Figs. 2 and S3) were obtained by adding a second water to each of $HisH^+(H_2O)$ structure depicted in Fig. S3. The most stable dihydrate, $HisH^+(H_2O)_2$_1 with a population of 89%, has two waters bound to -OH and -$N^{\tau}$H, respectively.

**3.1.2 $[His\text{-}H]^-(H_2O)_{n=0\text{-}2}$.** Deprotonation of His leads to three structures denoted $[His^{\tau}\text{-}H_{ca}]^-$, $[His^{\pi}\text{-}H_{ca}]^-$ (*i.e.* the τ and π tautomers deprotonated at -COOH), and $[His\text{-}H_{im}]^-$ (deprotonated at imidazole -NH), respectively. We have envisaged more than 150 trial conformations originating from these structures and obtained 27 stable tautomers/conformers at the B3LYP and MP2 levels (summarized in Fig. S4), many of which have not been reported in literature.[24,59, 66] The most stable deprotonated conformations belong to the $[His^{\pi}\text{-}H_{ca}]^-$ category, of which the first four low-lying conformers are illustrated in Fig. 2. Their B3LYP/6-311++G(d,p) calculated percentage populations are 57, 40, 2 and 1, respectively.

In contrast to $HisH^+$ hydrates which maintain the original conformations of bare ions, $[His\text{-}H]^-$ may undergo a big conformational change upon hydration. We added a water to structures of $[His^{\pi}\text{-}H_{ca}]^-$, $[His^{\tau}\text{-}H_{ca}]^-$ and $[His\text{-}H_{im}]^-$ identified, so as not to overlook stable hydrated structures resulting from any $[His\text{-}H]^-$ tautomers. A total of thirteen stable conformations were identified for $[His\text{-}H]^-(H_2O)$ (see Fig. S5). Their hydration energies were calculated with respect to the corresponding dehydrated structures. The -$COO^-$, -$NH_2$, -$N^{\tau}$, and -$N^{\pi}$ sites can each provide $E_{hydration}$ of 0.69, 0.50, 0.52 and 0.44 eV, respectively. $[His\text{-}H]^-(H_2O)$_1, which undergoes bidentate complexation and forms two hydrogen bonds between water and -$COO^-$, predominates at 298 K with a population of 97%.

Starting geometries of $[His\text{-}H]^-(H_2O)_2$ were created by combining any two of the hydration sites identified in $[His\text{-}H]^-(H_2O)$, and all optimized conformers are depicted in Fig. S5. Only the first four lowest-energy conformations (cf. Figs. 2 and S5) have significant populations (78%, 8%, 7% and 4%, respectively).

### 3.2 Missing oxidation products for bare His

The first striking observation from gas-phase experiments is that neither of bare $HisH^+$ and $[His\text{-}H]^-$ was oxidized by $^1O_2$. No oxidation products were observed for these two systems, except small amount of *m/z* 128 from $HisH^+ + {}^1O_2$ at high $^1O_2$ gas pressure where multiple collisions prevailed. At high $E_{col}$ collision-induced dissociation (CID) product ions were observed due to elimination of $NH_3$, $H_2O$, $H_2O$ + CO (concomitant loss), $NH_3 + CO_2$, $H_2O + CO + NH_3$, and $NH{=}CHCO_2H$ from $HisH^+$,[60, 67-70] and elimination of $NH_3$, $H_2O$, CN, $CO_2$, $HCO_2H$, $NH_3 + CO_2$, $C_4H_6N_2$ from $[His\text{-}H]^-$.[67]

To explore the origin of non-reactivity of bare His ions, we have mapped out potential energy surfaces (PESs) associated with their reaction coordinates. For $HisH^+ + {}^1O_2$, we have constructed two PESs starting from $HisH_{im}^+\_1$ and $His^{\tau}H_{am}^+\_2$, respectively. It was found that two PESs are almost identical, therefore only the one of $HisH_{im}^+\_1$ is displayed in Fig. 3a. We have excluded the intersystem crossing of $^1O_2 + {}^1HisH^+ \rightarrow {}^3O_2 + {}^3HisH^+$ in the PES since it is 2.44 eV endothermic. To avoid the problem of mixed open- and closed-shell characteristics of $^1O_2$ in energy calculation,[71] the DFT energy of $^1O_2$ was obtained by adding experimental excitation energy (0.98 eV) to the DFT energy of $^3O_2$.

As illustrated in Fig. 3a, a weakly bound precursor complex and several covalently bound complexes may form for $HisH^+ + {}^1O_2$. We have located TSs connecting the complexes to each other and to the products. The precursor complex is formed by electronic interaction with a binding energy of only ~0.1 eV. The precursor is rather floppy, with large amplitude of intermolecular motion. It allows repeated encounters between reactants, increasing the probability of crossing TS1 to 2,5- endoperoxide through [4+2] cycloaddition. The ″conjugated diene″ portion of $HisH^+$ is centered at C2=N3-C4=C5 (indicated in red in the ChemDraw structure in Fig. 3a), therefore [4+2] cycloaddition occurs across C2-C5 and

produces 2,5-endoperoxide HisH-2,5-$OO^+$. We have checked the possibility of forming 2,4-endoperoxide by running a relaxed potential energy scan along the approaching of one O atom toward C4. The rO-C4 bond length was continuously varied, and all other coordinates were optimized at each point. As expected, the relaxed scan avoided cycloaddition to C2-C4 and instead converged to HisH-2,5-$OO^+$.

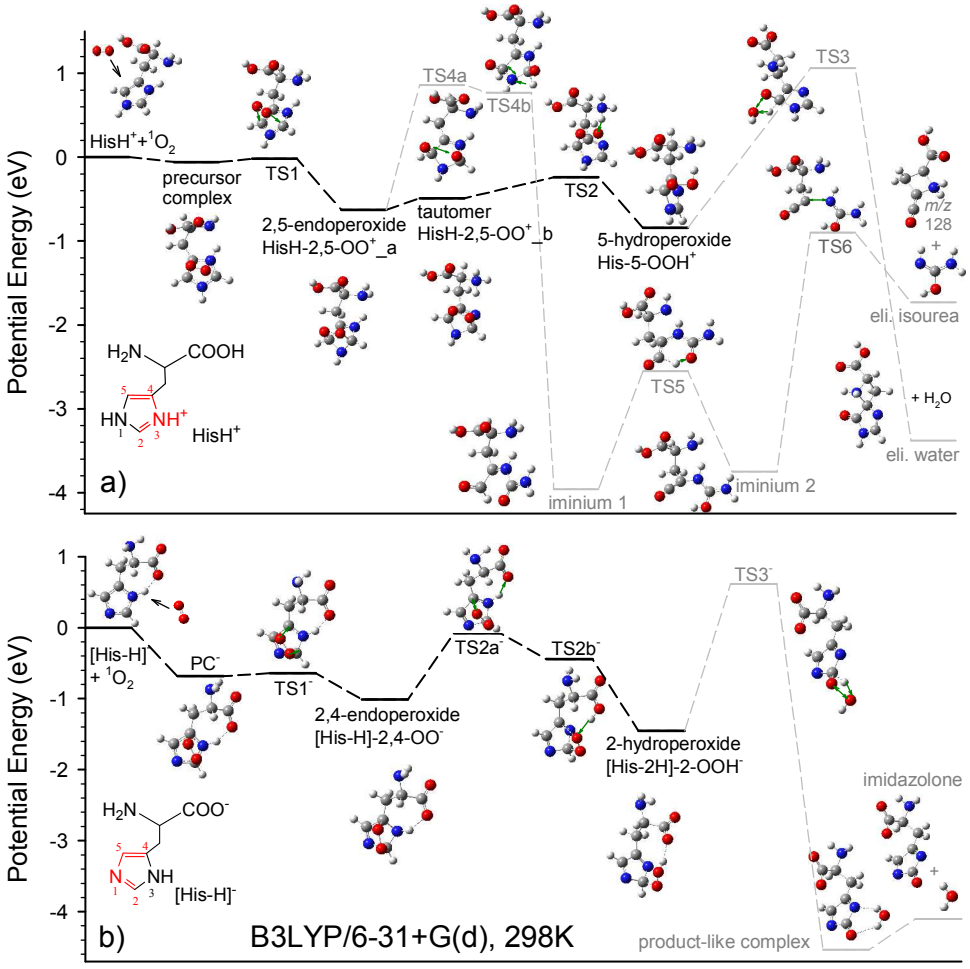


**Fig. 3** Reaction coordinates for the reactions of $^1O_2$ with a) $HisH^+$ and b) $[His\text{-}H]^-$. Favorable pathways are indicated by heavy dashed lines. Transition vectors in each TS are indicated by green arrows.

HisH-2,5-$OO^+$ has two prototropic tautomers: HisH-2,5-$OO^+$_a ($N^\pi$-protonated) and b ($N^\alpha$-protonated) with binding energies of 0.63 and 0.49 eV, respectively. HisH-2,5-$OO^+$ may open the ring and interconvert to His-5-$OOH^+$. The rearrangement is facilitated by temporary protonation of the amino group with the $N^\pi$ proton (*i.e.* HisH-2,5-$OO\_a^+ \rightarrow$ HisH-2,5-$OO^+$_b), followed by dissociation of the O-

C2 bond and in the meantime transfer of the proton from -$NH_3^+$ to the peroxide terminal (TS2). The interconversion barrier leading to His-5-$OOH^+$ is 0.25 eV above HisH-$OO^+$_b. It is possible that HisH-2,5-$OO^+$ breaks the O-C5 bond and rearranges to 2-hydroperoxide; however, the corresponding TS is 1.19 eV above HisH-2,5-$OO^+$_b (or 0.70 eV with respect to reactants), and thus is not energetically feasible.

The mechanistic importance of the precursor, HisH-2,5-$OO^+$ and His-5-$OOH^+$ depends on their dissociation kinetics and lifetimes, so we have used RRKM theory to calculate the rates for all unimolecular channels leading from these complexes as indicated in the PES. HisH-2,5-$OO^+$ and His-5-$OOH^+$ carry high internal energy, and therefore are destined to fragmentation. One possible decomposition pathway is 1,2-elimination of water from His-5-$OOH^+$ and subsequent internal cyclization, producing a bicyclic ketonic compound (via TS3).[25] The other option is return to reactants, *i.e.* non-reactive. No barrier is expected for decay of the precursor back to reactants in excess of the asymptote, thus an orbiting TS[72] was assumed. Rotation quantum number $K$ was treated as active in evaluating $k(E, J)$ so that all $(2J+1)$ $K$-levels are counted,[73] *i.e.*,

$$k(E,J) = \frac{d}{h}\frac{\sum_{K=-J}^{J} G(E - E_0 - E_r^+(J,K)]}{\sum_{K=-J}^{J} N[E - E_r(J,K)]} \qquad (1)$$

where $d$ is reaction path degeneracy, $G$ is the sum of states from 0 to $E$ - $E_0$- $E_r^\dagger$ at TS, $N$ is reactant density of states, $E$ is the system energy, $E_0$ is unimolecular dissociation threshold, and $E_r$ and $E_r^\dagger$ are the rotational energies for the reactant and the TS, respectively. Orbital angular momentum $L$ was estimated from collision cross section.

Analysis of RRKM results provides several insights. First, the dominant decay channel for the precursor corresponds to ″back to reactants″, and the branching ratio to HisH-2,5-$OO^+$ is < 1% even at lowest $E_{col}$ and decreases with $E_{col}$. This is because TS1 is tighter than the orbiting TS governing dissociation back to reactants. Second, inhibited by the high exit barrier TS3 (1.1 eV above the reactants), neither of HisH-2,5-$OO^+$ and His-5-$OOH^+$ (if formed) could convert to any stable end-products but

starting molecules. Third, the lifetime of HisH-2,5-$OO^+$ and His-5-$OOH^+$ is around psec, much shorter than the ion time-of-flight within the octopole and the second mass filter (~10 μsec). Consequently, HisH-2,5-$OO^+$ and His-5-$OOH^+$ were barely detectable in product mass spectra.

PES also suggests a route for product ions of *m/z* 128, *i.e.*, reactants → precursor → TS1 → HisH-2,5-$OO^+$_a → TS4a/b → iminium 1 → TS5 → iminium 2 → TS6 → four-membered ring product (*m/z* 128) + *iso*-urea. This pathway is endothermic, occurring only at high $E_{col}$ or under multiple collisions.

PES for [His-H]$^-$ + $^1O_2$ is shown in Fig. 3b. To facilitate the comparison of the two PESs of different ionization states, all corresponding critical structures are assigned with identical names but with negative superscript in the acronyms for the deprotonated ones. Similar to the protonated case, the reaction of [His-H]$^-$ first forms endoperoxide via [4+2] cycloaddition. In contrast to $HisH^+$, the ″conjugated diene″ of [His-H]$^-$ locates at imidazole C2=N1-C5=C4, so [4+2] cycloaddition occurs across C2-C4 leading to HisH-2,4-$OO^-$. We thought it might be possible to have structure resonance during the reaction and produce 2,5-endoperoxide [His-H]-2,5-$OO^-$. But various starting geometries of [His-H]-2,5-$OO^-$ all converged to [His-H]-2,4-$OO^-$ at the B3LYP and MP2 levels. [His-H]-2,4-$OO^-$ may rearrange to 2-hydroperoxide [His-2H]-2-$OOH^-$ through two step: first, [His-H]-2,4-$OO^-$ breaks the O-C4 bond and loans its $N^{\pi}$ proton to -$COO^-$ (TS2a$^-$); then this proton is transferred to the peroxide group (TS2b$^-$). Consecutive TS2a$^-$/b$^-$ sum up to 0.93 eV with respect to [His-H]-2,4-$OO^-$. The TS leading to the dissociation of the O-C2 bond has a much higher barrier (2.3 eV above [His-H]-2,4-$OO^-$, not shown in the PES), we can therefore rule out the formation of 4-hydroperoxide of [His-H]$^-$. Finally, as the $HisH^+$ system, neither endo- or hydro-peroxide of [His-H]$^-$ is able to survive intact (due to short lifetime), or evolve to stable products (due to the high lying TS3$^-$ located in the product exit channel).

In sum, the oxidation of $HisH^+$ is mediated by 2,5-endoperoxide and 5-hydroperoide, while that of [His-H]$^-$ is by 2,4-endoperoxide and 2-hydroperoxide. The consequence of the mechanistic difference between $HisH^+$ and [His-H]$^-$ seems not obvious here as no stable end-products were observed. But such difference results in distinctly different pathways and products as systems become hydrated (*vide infra*).

The non-reactive nature of bare His ions was verified by dynamics simulations. A typical trajectory of $HisH^+ + {}^1O_2$ is demonstrated in Fig. 4. In this trajectory, ${}^1O_2$ first approaches $HisH^+$ backbone, forming a loosely bound precursor as shown by the decrease of the CM distance (*i.e.* the distance between the centers of the mass of reactants) to less than 5 Å. After initial collision, the precursor undergoes repeated separation/recombination and structure interconversion between the collision partners, including prototropic tautomerism between $N^{\alpha}$ and $N^{\pi}$ (see the snapshots at t = 0 and 382 fsec). This is followed by the formation of HisH-2,5-$OO^+$ at 2975 fsec. HisH-2,5-$OO^+$ has a very brief interconversion with hydroperoxide. The rO-O′, rO-C2 and rO′-C5 bond lengths plotted in the figure correspond to the bond length of $O_2$ moiety and two O-C bonds being formed in 2,5-endoperoxide, respectively; and the profiles of $rN^{\alpha}$-H and $rN^{\pi}$-H represents the prototropic tautomerism in the reactant and the intermediate. The oscillation in bond lengths and PE reflect the vibrations of the reactants and intermediates, including ZPE. The total lifetime of HisH-2,5-$OO^+$ accounts for only ~1 psec of trajectory time. The system decays back to reactants before the trajectory termination, consistent with the RRKM-predicted dissociation kinetics.

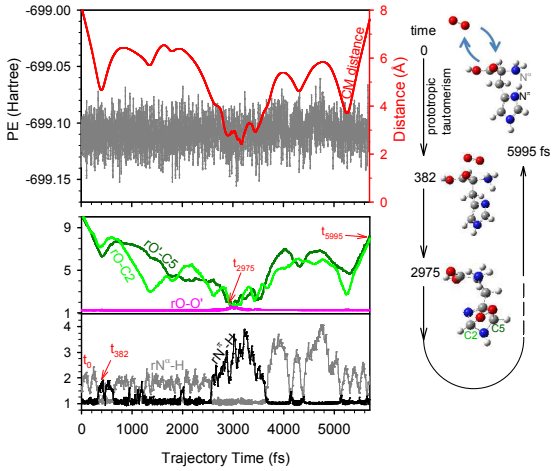


**Fig. 4** A representative trajectory of $HisH^+ + {}^1O_2$ simulated at $E_{col}$ = 0.1 eV. Top: the variation of potential energy and the CM distance between reactant moieties. Bottom: the variation of various bond lengths. Snapshots show representative events along trajectory time.

### 3.3 Microsolvation introduces intrinsic changes in reactions

**3.3.1 Capturing stable oxidation products in hydrates.** Statistical modeling and dynamics simulations

have shown that the oxidation of $HisH^+$ and $[His\text{-}H]^-$ produced a mixture of endoperoxides and hydroperoxides, yet these intermediates ultimately decomposed to starting reactants. This raises questions on the actual roles of *endoperoxides and hydroperoxides in His oxidation and how they contribute to end-products.* Clues were found in the reactions of hydrates, as stable oxidation products were indeed detected in the $^1O_2$ reactions with $HisH^+(H_2O)_{1,2}$ and $[His\text{-}H]^-(H_2O)_{1,2}$.

Oxidation product ions for the reaction of $HisH^+(H_2O)$ (*m/z* 174) + $^1O_2$ were observed at *m/z* 188, which can be attributed to the formation of a peroxide of $HisH^+$. For the reaction of $HisH^+(H_2O)_2$ (*m/z* 192) + $^1O_2$, oxidation product ions were observed at *m/z* 224, 206, and 188. *m/z* 188 has the same origin as that observed in the reaction of monohydrated $HisH^+$, and *m/z* 224 and 206 correspond to di- and monohydrated peroxides, respectively; albeit that *m/z* 224 was observed only at lowest $E_{col}$ and with insignificant intensity. Reaction cross sections and efficiencies ($= \sigma_{total}/\sigma_{collision}$) for $HisH^+(H_2O)_{1,2}$ + $^1O_2$ are shown in Fig. 5a and b as a function of $E_{col}$. Both reactions present exothermic behavior — their cross sections increase with decreasing $E_{col}$, indicating that there are no activation barriers above reactants.

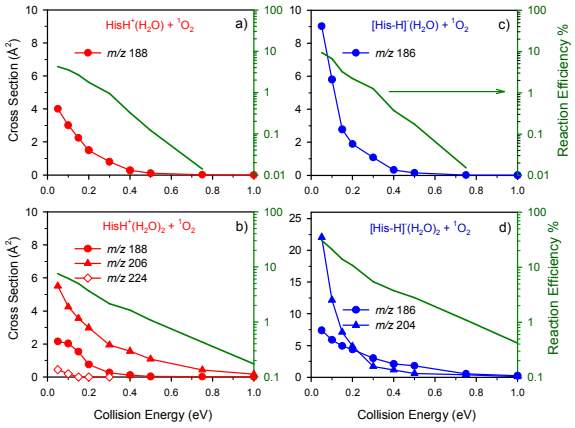


**Fig. 5** Product cross sections for the reactions of $^1O_2$ with a) $HisH^+(H_2O)$, b) $HisH^+(H_2O)_2$, c) $[His\text{-}H]^-(H_2O)$, and d) $[His\text{-}H]^-(H_2O)_2$, as a function of center-of-mass $E_{col}$. Reaction efficiencies (dark green curves) are shown on the right axis using log scale.

$^1O_2$-specific peroxide product ions were observed at *m/z* 186 for the reaction of $[His\text{-}H]^-(H_2O)$ (*m/z* 172) + $^1O_2$, and at *m/z* 204 and 186 for that of $[His\text{-}H]^-(H_2O)_2$ (*m/z* 190) + $^1O_2$. Their reaction cross

sections and efficiencies as well as $E_{col}$ dependence are shown in Fig. 5c and d. Similar to $HisH^+(H_2O)_{1-2}$, the reactions of $[His\text{-}H]^-(H_2O)_{1,2}$ are strongly inhibited by $E_{col}$, becoming negligible at $E_{col} > 0.5$ eV. However, at low-$E_{col}$ regime ($\leq 0.1$ eV), the efficiency of $[His\text{-}H]^-(H_2O)$ increases by two times and that of $[His\text{-}H]^-(H_2O)_2$ increases by four times compared to their protonated counterparts.

Note that the B3LYP/6-311++G(d,p) calculated electron detachment energies for $[His\text{-}H]^-$, $[His\text{-}H]^-(H_2O)$ and $[His\text{-}H]^-(H_2O)_2$ are 3.04, 3.50 and 3.72 eV, respectively, which is beyond the $E_{col}$ range of 0.05 - 1.0 eV used in our experiment. Consequently, collision-induced detachment of an excess electron from negative $[His\text{-}H]^-(H_2O)_{0-2}$ could be ignored. In addition, assuming the excitation energy (0.98 eV)[39] and electron affinity (0.45 eV)[74] of $^1O_2$ can be used to drive electron transfer between $[His\text{-}H]^-(H_2O)_{0-2}$ and $^1O_2$, these reactions are endothermic by > 1.61 eV and thus cannot occur in the present $E_{col}$ range.

**3.3.2 Reaction pathways move forward with addition of water(s).** We first focus on the PES for the reaction of monohydrated $HisH^+(H_2O)$ with $^1O_2$, as illustrated in Fig. 6a (a water ligand was included in the acronyms for critical structures). The gross feature of the early stage PES for $HisH^+(H_2O) + {}^1O_2$ is similar to that of $HisH^+ + {}^1O_2$. RRKM predicts that the branching ratio for interconversion of PC(W) to endoperoxide HisH-2,5-$OO^+$(W)_a is 5% at $E_{col} = 0.05$ eV. HisH-2,5-$OO^+$(W)_a evolves along two pathways. The dominant pathway is HisH-2,5-$OO^+$(W)_a $\rightarrow$ HisH-2,5-$OO^+$(W)_ b $\rightarrow$ TS2(W) $\rightarrow$ His-5-$OOH^+$(W) $\rightarrow$ His-5-$OOH^+$ (*m/z* 188) + water (overall reaction heat of formation $\Delta H_r = -0.23$ eV). Other minor pathway might be HisH-2,5-$OO^+$(W)_a $\rightarrow$ HisH-2,5-$OO^+$ (*m/z* 188) + water ($\Delta H_r = -0.02$ eV). The system spends most of the collision time at ensuing His-5-$OOH^+$(W), before its overwhelming dissociation to stable His-5-$OOH^+$ and a separate water. Accordingly, we can estimate a total reaction efficiency of ~5% at the lowest $E_{col}$, which is in a nice agreement with the ion-beam experiment.

The PES associated with low energy pathways for $[His\text{-}H]^-(H_2O) + {}^1O_2$ is presented in Fig. 6b. The reaction follows reactants $\rightarrow$ $PC^-$(W) $\rightarrow$ $TS1^-$(W) $\rightarrow$ [His-H]-2,4-$OO^-$(W). [His-H]-2,4-$OO^-$(W) either dissociates to [His-H]-2,4-$OO^-$ (*m/z* 186) + water ($\Delta H_r = -0.39$ eV), or rearranges to [His-2H]-2-$OOH^-$(W) (with a barrier $TS2^-$(W) of 0.23 eV below the reactants) followed by water elimination to [His-2H]-2-

$OOH^-$ (*m/z* 186). RRKM suggests the first route dominates at low $E_{col}$, resulting in [His-H]-2,4-$OO^-$ as the major product over [His-2H]-2-$OOH^-$ (which is opposite to $HisH^+(H_2O) + {}^1O_2$ where His-5-$OOH^+$ is the major product). PESs for the reactions of $HisH^+(H_2O)_2$ and $[His\text{-}H]^-(H_2O)_2$ are presented in Fig. S6 and discussed in the supporting information. They follow similar routes as their monohydrates.

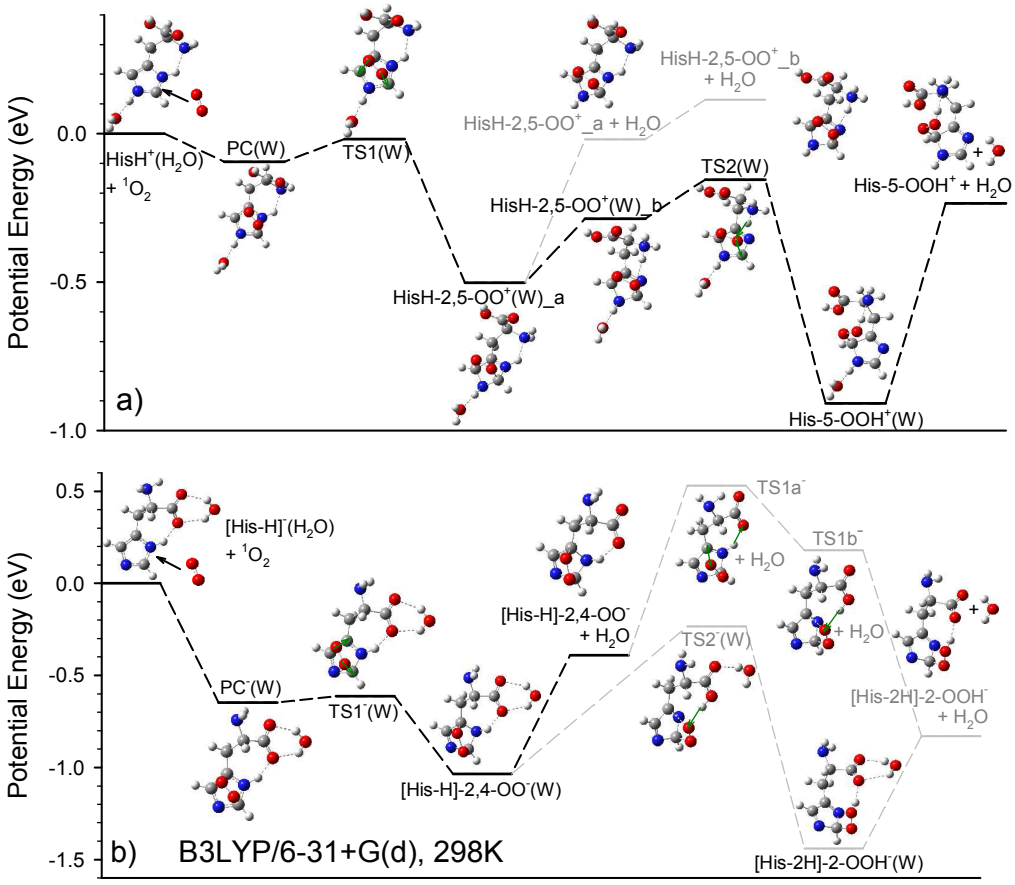


**Fig. 6** Schematic reaction coordinates for a) $HisH^+(H_2O) + {}^1O_2$ and b) $[His\text{-}H]^-(H_2O) + {}^1O_2$. Favorable pathways are indicated by heavy dashed lines. Transition vectors in each TS are indicated by green arrows.

**3.3.3 Dynamical roles of water.** The key to unraveling non-reactivity of dry $HisH^+$/$[His\text{-}H]^-$ *vs.* medium to high reactivity of mono- and dihydrates lies in the fact that the hydrates provide a mechanism by which ″hot″ endoperoxide and hydroperoxide intermediates can remove internal excitation via cluster dissociation and become stabilized with respect to fragmentation. Single water dissociation energies are

0.48-0.67 eV for the monohydrates of protonated/deprotonated intermediates, and 0.42-0.58 eV for the dihydrates of protonated/deprotonated intermediates, all of which are below the dissociation thresholds of the corresponding peroxide moieties. Water dissociation and accompanying product kinetic energy release open an efficient relaxation pathway for nascent endoperoxide and hydroperoxide. In this context, a single water is capable of changing the oxidation pathways intrinsically.

The proposed scenario is supported by a typical trajectory of $[His\text{-}H]^-(H_2O) + {}^1O_2$, depicted in Fig. 7. The top frame of the figure plots the PE, the $O_2$ bond length, and the CM distances between $O_2$ and $[His\text{-}H]^-$ and between water and $[His\text{-}H]^-$. The bonds plotted in the bottom frame correspond to the two new C-O bonds being formed in $[His\text{-}H]\text{-}2,4\text{-}OO^-(H_2O)$. Formation of $[His\text{-}H]\text{-}2,4\text{-}OO^-(H_2O)$ occurs at 778 fsec, followed by water elimination at 3 psec. By the end of the trajectory, water is separated from the stable 2,4-endoperoxide by ~7 Å.

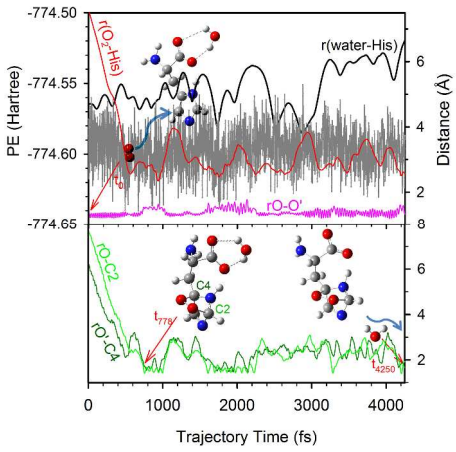


**Fig. 7** A representative trajectory of $[His\text{-}H]^-(H_2O) + {}^1O_2$ at $E_{col} = 0.1$ eV, showing the variation of potential energy, the CM distances between reactant moieties and various bond lengths during trajectory. Snapshots show representative events.

Table 1 summarizes the experimental measured reaction efficiencies for dry, mono- and dihydrated systems. As shown in Table 1, dihydrated $HisH^+(H_2O)_2$ and $[His\text{-}H]^-(H_2O)_2$ have higher reaction efficiencies than their monohydrated analogues. This observation might be mainly attributed to the fact that the second water is less strongly bound than the first water. Dihydrates therefore have a lower energy

dissociation channel to eject a water than monohydrates. These findings reinforce the understanding that gas-phase hydrated AAs involve individual solute-solvent dynamics and their coupling, rather than simply AA dynamics under the influence of some representation of the solvent.[35]

**Table 1** Reaction efficiencies, binding energies and bond indexes of His···$^1O_2$ precursors, and products

| $E_{col}$ / eV | Reaction Efficiency% | | Binding energy (eV) / Wiberg index of precursor complex | | | Products | |
|---|---|---|---|---|---|---|---|
| | $HisH^+$ | $[His\text{-}H]^-$ | $HisH^+$ | His | $[His\text{-}H]^-$ | $HisH^+$ | $[His\text{-}H]^-$ |
| 0.05-1.0 | 0 | 0 | 0.05 / 0.08 | 0.35/0.14 | 0.68 / 0.18 | None | None |
| | $HisH^+(H_2O)$ | $[His\text{-}H]^-(H_2O)$ | $HisH^+(H_2O)$ | $His(H_2O)$ | $[His\text{-}H]^-(H_2O)$ | $HisH^+(H_2O)$ | $[His\text{-}H]^-(H_2O)$ |
| 0.05 | 4.2 | 9.5 | 0.10 / 0.09 | 0.31/0.13 | 0.65 / 0.18 | 2,5-endoperoxide +5-hydroperoxide (major) | 2,4-endoperoxide (major) + 2-hydroperoxide |
| 0.1 | 3.5 | 6.7 | | | | | |
| 0.2 | 1.7 | 2.2 | | | | | |
| | $HisH^+(H_2O)_2$ | $[His\text{-}H]^-(H_2O)_2$ | $HisH^+(H_2O)_2$ | $His(H_2O)_2$ | $[His\text{-}H]^-(H_2O)_2$ | $HisH^+(H_2O)_2$ | $[His\text{-}H]^-(H_2O)_2$ |
| 0.05 | 7.5 | 30.8 | 0.09 / 0.09 | 0.32/0.13 | 0.62 / 0.18 | 2,5-endoperoxide +5-hydroperoxide (major) | 2,4-endoperoxide (major) + 2-hydroperoxide |
| 0.1 | 6.1 | 21.1 | | | | | |
| 0.2 | 3.7 | 10.8 | | | | | |

A complication in thinking about the reactions of hydrates with $^1O_2$ is that the excitation energy of $^1O_2$ may be used to dissociate ionic water clusters.[75] We were not able to distinguish in the experiment if water elimination of hydrates occurred by CID or dissociative excitation transfer. However, trajectory simulations of $HisH^+(H_2O) + {}^1O_2$ show that at $E_{col} = 0.1$ eV only less than 17% of collisions have $^1O_2$ attack the water ligand directly. Viggiano *et al.*[75] demonstrated that in the reaction of $OH^-(H_2O) + {}^1O_2$ the excitation transfer-induced water dissociation is direct. Assuming the direct mechanism is the case for His ionic hydrates, only a fraction of the 17% direct water-attack collisions may quench $^1O_2$ by dissociative excitation transfer. In addition, while the dissociative excitation transfer with $HisH^+(H_2O)_{1,2}$ and $[His\text{-}H]^-(H_2O)_{1,2}$ should be exothermic, the measured cross sections for water elimination of $HisH^+(H_2O)_{1,2}$ and $[His\text{-}H]^-(H_2O)_{1,2}$ have an endothermic $E_{col}$ dependence. We therefore conclude that dissociative excitation transfer is not a major path in our systems.

**3.3.4 Mimicking photooxidation pH dependence.** Another interesting finding from the reactions of hydrates is that the reactivity of deprotonated hydrates is much higher than that of protonated ones. Table

1 shows that the reaction efficiency of $[His\text{-}H]^-(H_2O)$ is 2-fold higher than that of $HisH^+(H_2O)$, and the efficiency of $[His\text{-}H]^-(H_2O)_2$ is 4-folder higher than that of $HisH^+(H_2O)_2$. This mimics the pH dependence observed in the photooxidation of His.[19-23] The origin of such reactivity difference could be traced back to the binding strength of the precursor complexes, and the ionization state of the imidazole ring.

As listed in Table 1, binding energies of protonated precursors are 0.5-0.6 eV lower than those of deprotonated ones. To compare the ionized species with neutral ones, values for the neutral systems are also included in the Table. Neutral precursors have medium binding energies between two ionized states. We have inspected the Wiberg bond indexes[76] between O atoms and their closest imidazole C atoms in precursor complexes. Average bond order is only 0.09 in protonated precursor complexes, increasing to 0.14 in neutral and 0.19 in deprotonated precursors. Consequently, protonated precursor complexes have much weaker interactions between reactants, and prefer to decay back to reactants by orbiting TSs rather than interconversion to covalently bound endoperoxides via tighter TSs. Moreover, the ensuing 2,5-endoperoxides of $HisH^+(H_2O)_n$ are also 0.5 eV less stable than 2,4-endoperoxides of $[His\text{-}H]^-(H_2O)_n$, and have a higher probability to regenerate starting molecules.

We may think about the correlation between His ionization state and its reactivity from another perspective. In typical Diels-Alder [4+2] cycloaddition, conjugated dienes are electron rich while dienophiles are electron poor. The portion of ″conjugated diene″ is C2=N1-C5=C4 in $[His\text{-}H]^-$ *vs.* $C2=N3^{\oplus}\text{-}C4=C5$ in $HisH^+$. The N1 lone pair in $[His\text{-}H]^-$ acts as electron releasing group and hence facilitates cycloaddition. In contrast, the protonated N3 in $HisH^+$ lowers π-electron density and must be responsible for low reactivity toward cycloaddition. We have calculated NBO[77] charge transfer between reactant moieties in various precursors. They are -0.15 in $HisH^+\cdots O_2$, -0.30 in $His\cdots O_2$, and -0.42 in $[His\text{-}H]^-\cdots O_2$. The sheer increasing of negative charge at $O_2$ from protonated to neutral and deprotonated systems indicates better electron donor properties of the unionized imidazole in His and $[His\text{-}H]^-$.

### 3.4 Fates of endoperoxides and hydroperoxides in aqueous solution

It is of much interest to us how the reaction profiles and products of gas-phase hydrates relate to

aqueous reactions. Note that in addition to the dynamic impact of intimate water ligands (as a reaction catalyst), an aqueous continuum results in solute polarization and stabilizes intermediates and TSs relative to reactants (given the non-polar nature of $^1O_2$). But such solvent effects do not change critical structures dramatically, as illustrated in the PES for the photooxidation of neutral His in aqueous solution.[25]

**3.4.1 pH-dependent kinetics.** Real-time UV-Vis absorption spectra allow for evaluating oxidation kinetics of His by following the change of solution absorption over the course of reaction. We have performed groups of UV-Vis analysis in the pH range of 4 - 12. As shown in Fig. S7, the oxidation of His presents remarkable pH-dependence in aqueous solution.[19-23] Note that in our solution experiment, $^1O_2$ was continuously bubbled into water solution; however, $^1O_2$ has only a ~150 nm diffusion distance in water,[78] which restricts its ability to diffuse from the gas/liquid interface of bubbles into bulk solution. As a result most of the $^1O_2$ reactions occurred at the liquid/gas interface. At each pH higher than 8, a linear relationship between $\ln(A_t/A_0)$ and reaction time $t$ was observed during the first 10-15 minutes of the reaction, where $A_t$ and $A_0$ are the peak absorbance of His at any time and time zero, respectively. This suggests that the early stage oxidation of His follows first-order kinetics, without significant second-order mechanisms. It can also be inferred from first-order kinetics that a quasi-steady-state concentration of $^1O_2$ was produced for our aqueous reactions.

**3.4.2 End-products and His cross-linking.** More detailed and informative results were obtained by on-line ESI MS monitoring of the reaction solution. Mass spectra of acidic and neutral solutions were measured in positive ion mode, while those of basic solutions were measured in negative mode. To avoid the interference of buffer ions in ESI, solution pH was adjusted by adding HCl or NaOH to 0.5 mM His aqueous solution, except for that of pH 7.4 which was maintained by the buffering effect of His itself. At pH < 7 no oxidation products were detected, in agreement with the UV-Vis results.

Fig. 8 demonstrate two MS measurements obtained at pH 7.4 (recorded in positive ion mode) and 10.4 (negative ion mode), respectively. $^1O_2$-specific products are indicated in red- and blue-shaded peaks in mass spectra. At pH 7.4 only one product was observed at *m/z* 188, corresponding to $HisH^+/O_2$ adduct.

At pH 10.4, besides $[His\text{-}H]^-/O_2$ adduct at *m/z* 186, products were detected at *m/z* 161 and 323. All reactions were monitored by ESI MS up to 1 hr. Under both pH conditions, the intensities of product ions increase with reaction time. Reaction rate at pH 10.4 is much faster than that at pH 7.4, which is again consistent with the pH dependence observed in the UV-Vis analysis.

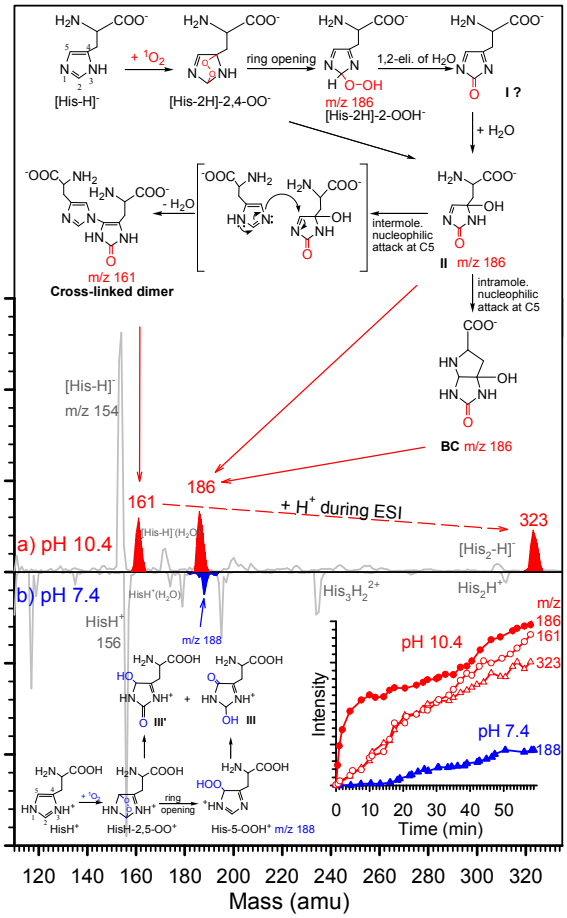


**Fig. 8** Mass spectra and mechanistic schemes for His oxidation in a) pH 10.4 and b) pH 7.4 solution. Reactant mass spectra are shown in gray color, and product ions are indicated in color shaded peaks. Insert: evolution of various products as a function of reaction time.

**3.4.3 Evolution of dynamics/products in aqueous solution.** Before discussing aqueous reaction mechanisms, it is useful to present a brief survey of relevant results and puzzles from previous photooxidation study of His. Formation of 2,5-endoperoxide in the photooxidation of His was verified using NMR.[17] This 2,5-endoperoxide was stable only at -100 °C, and decomposed to reactants (or

rearranged to hydroperoxide) once the temperature rose to -88 °C. Hydroperoxide was proposed to form from the ring opening of 2,5-endoperoxide at either C2-O or C5-O bond, resulting in 2- and/or 5-hydroperoxide. Hydroperoxide was detected at ambient temperature and pH 7.4,[18] based on a modified ferrous oxidation-xylenol orange (FOX) assay. However, this approach was not able to distinguish 2- and 5-hydroperoxides. Note that the fates of 2- and 5-hydroperoxides are different. 2-hydroperoxide, if formed, may eliminate a water molecule and then undergo hydration at one of the two imine sites, yielding hydrated imidazolone analogue. The latter contains an electrophilic locus at C5, which may be attacked readily by the backbone amino through intramolecular nucleophilic cyclization, producing a bicyclic product 6α-hydoxy-2-oxo-octahydro-pyrrolo[2,3-d]imidazole-5-carboxylic acid (neutral form of **BC** in Fig. 8). The similar 1,2-water elimination and rehydration process, if occurs to 5-hydroperoxide, results in the formation of another hydrated imidazolone (denoted **III** in Fig. 8), which is not susceptible to nucleophilic attack and thus could not produce a **BC**-like product. It is also worth noting that Tomita *et al.* identified dimeric species in the photooxidation of *N*-benzoyl-His at pH 11.[15] This dimeric product was assumed to be formed via intermolecular nucleophilic attack of the above-mentioned hydrated imidazolone by another *N*-benzoyl-His at C5 and subsequent loss of water. Similar dimeric product was observed in the photooxidation of *N*-acetyl-His at pH 7.4,[18] but not in the photooxidation of His under the same conditions.[18] Combining our gas- and solution-phase findings and taking into account the photooxidation results, we are able to piece together solution-phase oxidation mechanisms for His, as depicted in the mechanistic schemes in Fig. 8 and detailed below.

**a) High reactivity in basic solution.** According to the reaction coordinates of $[His\text{-}H]^-(H_2O)_n$, we may reasonably propose that [His-H]-2,4-$OO^-$ was formed initially at basic pH. Based on NMR measurements of similar endoperoxides,[17] [His-H]-2,4-$OO^-$ should be very reactive at room temperature and quickly decomposed to [His-2H]-2-$OOH^-$. 1,2-water elimination of ensuing [His-2H]-2-$OOH^-$ would first lead to an intermediate **I** (*m/z* 168), which subsequently evolved to **II**. Since **I** is susceptible to intramolecular ring closure via nucleophilic attack at C5, a bicyclic product of *m/z* 168 would be formed from **I**; but it

was not observed. The absence of *m/z* 168 in Fig. 8a made us think that, instead of being mediated by **I**, [His-H]-2,4-$OO^-$ may break the peroxide bridge to form a hydrated imidazolone **II** directly in solution**,** and finally give rise to a **BC** product (6α-hydoxy-2-oxo-octahydro-pyrrolo[2,3-d]imidazole-5-carboxylate). Note that we did not consider the direct pathway from [His-H]-2,4-$OO^-$ to **II** in gas-phase reactions, because the dissociation of an O-O bond involves a barrier of ~1 eV; but it may happen in solution if surroundings provide sufficient energy.

The product peak we observed at *m/z* 186 might be assigned to a mixture of [His-2H]-2-$OOH^-$**,** **II** and **BC**. **II** could be further attacked by another His followed by water elimination to give a cross-linked dimer at *m/z* 161. During ESI, doubly charged dimer might gain a proton and convert to a singly charged ion at *m/z* 323. As a result, products of *m/z* 161 and 323 have the same origins, and present similar growing curves over the course of the reaction (see Fig. 8 insert), with an approximate 1:1 ratio.

The above mechanism is supported by UV-Vis kinetic analysis and the time profiles of the products at pH 10.4. The first-order disappearance of His UV absorption and the fast rising in the intensity of *m/z* 186 within the first 10 minutes of the reaction is due to the dominating formation of [His-2H]-2-$OOH^-$ (and some **II)**. After that, the formation of **BC** via *intramolecular nucleophilic attack* and the formation of His-His dimers via *intermolecular nucleophilic attack* took place significantly. This is evidenced by the fact that the net formation of *m/z* 186 started to slow down from *t* = 10 min to 35 min. The formation rate of *m/z* 161 and 323 is determined by the concentration of **II**, and therefore showed a hysteresis at the beginning of the reaction. But there were more dimeric products (including *m/z* 161 and 323) produced than *m/z* 186 as the reaction reached equilibrium. The intensity ratio of 1:1.5 for *m/z* 186 and (*m/z* 161 + *m/z* 323) in the last product mass spectrum reflects the branching between *intramolecular* and *intermolecular* attacks at C5 of **II** by different nucleophiles.

As we calculated, the most stable deprotonated His has a structure of $[His^{\pi}\text{-}H_{ca}]^-$ with an H located at $N^{\pi}$, this is equivalent to the π tautomer of neutral imidazole. By comparing alkylation kinetics of the π *vs.* τ tautomers of *N*-Acetyl-His and *N*-Acetyl-His methylamide, Calleman *et al.* [79] claimed that the π

tautomer acts as a stronger base and thus a stronger nucleophile than the τ tautomer. This may also account for high His-His cross-linking reactivities observed in basic solution.

**b) Low efficiency in neutral solution.** In contrast against what happened to $[His-H]^-$ in basic solution, the oxidation of $HisH^+$ first led to unstable endoperoxide HisH-2,5-$OO^+$, subsequent decomposition of which gave rise to His-5-$OOH^+$ at *m/z* 188 in solution. 1,2-water elimination of His-5-$OOH^+$ and hydration of the ensuing imine yielded hydrated imidazolone **III**. As in the deprotonated case, direct ring-opening of HisH-2,5-$OO^+$ to **III** and its isomer **III'** might be possible in solution. The product of *m/z* 188 in Fig. 8 could be mainly attributed to His-5-$OOH^+$ (minor) and hydrated imidazolone **III** and **III'**. **III** and **III'** are stable against further nucleophilic attacks, because both [1,4] conjugate addition for dimerization and [1,4] addition from α-$NH_2$ become unfavorable due to site hindrance. Therefore, no other products or cross-linked species were detected at pH 7.4. The absence of His dimeric product at pH 7.4 is consistent with the stoichiometry reported at pH 7.0,[19] where a 1:1 molar ratio was found for $O_2$: His (the consumption of $O_2$ slightly increased at high temperatures, but no more than 1.2:1).

Note that although the product mass spectra of pH 7.4 were measured in positive ion mode, the resulting spectra probably reflect mixed behaviors of neutral and protonated His. The mechanistic scheme proposed for $HisH^+$ may apply to neutral His, in that case all structures are not protonated and have zwitterion backbone structures in the reaction scheme.

## 4 Conclusions

By using experimental and theoretical approaches, we have completed a parallel investigation of gas- and solution-phase $^1O_2$ oxidation of His, and are able to extract considerably detailed oxidation mechanisms in different hydrated media as well as their relevance. A common process to protonated and deprotonated His is the formation of endoperoxides via [4+2] cycloaddition, which may rearrange to hydroperoxides. Neither of endo- and hydro-peroxide intermediates is stable when His is dehydrated and isolated in the gas phase, but decays back to starting reactants. Dynamic effects of individual water molecules are demonstrated in the oxidation of the same gas-phase systems clustering with an explicit

number of water molecules. Dominant hydration effect is the suppression of intermediate dissociative pathways and production of stable peroxide products. This can be attributed to energy dissipation from excited intermediates via water cluster dissociation. Reaction potential energy surfaces, statistical modeling and dynamics simulations all support the predominant formation of 5-hydroperoxide for protonated His, and 2,4-endoperoxide for deprotonated His. In aqueous solution, protonated 5-hydroperoxide rearranges to hydrated imidazolone end-product; deprotonated 2,4-endoperoxide, on the other hand, interconverts to deprotonated 2-hydroperoxide. Both deprotonated 2,4-endoperoxide and 2-hydroperoxide may evolve to hydrated imidazolone compound, which undergoes either intramolecular nucleophilic attack to produce 6α-hydoxy-2-oxo-octahydro-pyrrolo[2,3-d] imidazole-5-carboxylate, or intermolecular nucleophilic attack by another His yielding His-His cross-linking. The reactivity of His toward $^1O_2$ is much higher in basic solution than in neutral and acidic solution. This pH dependence is correlated with imidazole tautomerism at varying pH, the interaction strength in reaction precursors, etc. Deprotonated His has a π tautomeric structure of the imidazole ring, this must be responsible for its high reactivity toward $^1O_2$.

It is worth mentioning the biological implications of these results. The $pK_a$ value of imidazole is 6.04. In some cases such as the ″Ser-His-Asp″ triad of chymotrypsin,[4] Asp is hydrogen bonded with His which increases imidazole $pK_a$ to ~12 and renders His a rather powerful base. Consequently, His exists in a mixture of neutral, protonated and deprotonated forms at physiological pH of ~7, and the two oxidation mechanisms we proposed are both important in biological systems. The other implication concerns $^1O_2$ oxidation of the guanine moiety of DNA, where the imidazole ring is again the target for oxidative damage and consequently photooxygenation is strongly pH dependent.[80, 81]

**Acknowledgements**

This work was supported by the National Science Foundation CAREER Award (Grant No. CHE-0954507) and PSC-CUNY Research Awards. We thank Pengfei Wang (UAB Chemistry) for his valuable comments on the manuscript.

**Electronic Supplementary Information:** Summary of literature proposed photooxidation mechanisms of histidine. Reactions of $^1O_2$ with $HisH^+(H_2O)_2$ and $[His\text{-}H]^-(H_2O)_2$. Supporting figures. Cartesian coordinates for stable conformers/tautomers of $HisH^+(H_2O)_{0,1,2}$ and $[His\text{-}H]^-(H_2O)_{0,1,2}$.

## References


1. J. C. Kendrew, R. E. Dickerson, B. E. Strandberg, R. G. Hart, D. R. Davies, D. C. Phillips and V. C. Shore, *Nature*, 1960, **185**, 422-427.
2. F. R. S. M. F. Perutz, M. G. Rossmann, A. F. Cullis, H. Muirhead, G. Will and A. C. T. North, *Nature*, 1960, **185**, 416-422.
3. A. Volbeda, M.-H. Charon, C. Piras, E. C. Hatchikian, M. Frey and J. C. Fontecilla-Camps, *Nature*, 1995, **373**, 580-587.
4. D. M. Blow, J. J. Birktoft and B. S. Hartley, *Nature*, 1969, **221**, 337-340.
5. M. J. Davies, *Biochem. Biophys. Res. Commun.*, 2003, **305**, 761-770.
6. C. S. Foote, in *Oxygen and Oxygen-Radicals in Chemistry and Biology*, eds. M. A. J. Rodgers and E. L. Powers, Academic Press, New York, 1981.
7. C. Schweitzer and R. Schmidt, *Chem. Rev.*, 2003, **103**, 1685-1757.
8. P. E. Morgan, R. T. Dean and M. J. Davies, *Eur. J. Biochem.*, 2002, **269**, 1916-1925.
9. H.-R. Shen, J. D. Spikes, C. J. Smith and J. Kopecek, *J. Photochem. Photobiol. A*, 2000, **130**, 1-6.
10. I. Kruk, *Environmental Toxicology and Chemistry of Oxygen Species* Springer, Berlin, 1998.
11. G. Palumbo, *Expert Opin. Drug Delivery*, 2007, **4**, 131-148.
12. K. Matsumoto and M. Uematsu, *Atmos. Environ.*, 2005, **39**, 2163-2170.
13. C. Anastasio and K. G. McGregor, *Atmos. Environ.*, 2001, **35**, 1079-1089.
14. K. G. McGregor and C. Anastasio, *Atmos. Environ.*, 2001, **35**, 1091-1104.
15. M. Tomita, M. Irie and T. Ukita, *Biochem.*, 1969, **8**, 5149-5160.
16. H.-S. Ryang and C. S. Foote, *J. Am. Chem. Soc.*, 1979, **101**, 6683-6687.
17. P. Kang and C. S. Foote, *Tetrehedron Lett.*, 2000, **41**, 9623-9626.
18. V. V. Agon, W. A. Bubb, A. Wright, C. L. Hawkins and M. J. Davies, *Free Radical Biology & Medicine*, 2006, **40**, 698-710.
19. L. Weil, *Arch. Biochem. Biophys.*, 1965, **110**, 57-68.
20. J. S. Bellin and C. A. Yankus, *Arch. Biochem. Biophys.*, 1968, **123**, 18-28.
21. T. Gomyo, Y. Yang and M. Fujimaki, *Agric. Biol. Chem.*, 1968, **32**, 1061-1069.
22. J. D. Spikes and M. L. MacKnight, *Ann. N. Y. Acad. Sci.*, 1970, **171**, 149-162.
23. I. B. C. Matheson and J. He, *Photochem. Photobiol.*, 1979, **29**, 879-881.
24. V. Riffet and G. Bouchoux, *Phem. Chem. Chem. Phys.*, 2013, **15**, 6097-6106.
25. J. Méndez-Hurtado, R. López, D. Suárez and M. I. Menéndez, *Eur. J. Chem.*, 2012, **18**, 8437-8447.
26. Y. Fang and J. Liu, *J. Phys. Chem. A*, 2009, **113**, 11250-11261.
27. Y. Fang, F. Liu, A. Bennett, S. Ara and J. Liu, *J. Phys. Chem. B*, 2011, **115**, 2671-2682.
28. F. Liu, Y. Fang, Y. Chen and J. Liu, *J. Phys. Chem. B*, 2011, **115**, 9898-9909.
29. F. Liu, Y. Fang, Y. Chen and J. Liu, *J. Phys. Chem. B*, 2012, **116**, 6369-6379.
30. Y. Fang, F. liu, R. Emre and J. Liu, *J. Phys. Chem. B*, 2013, **117**, 2878-2887.
31. W. Lu, F. Liu, R. Emre and J. Liu, *J. Phys. Chem. B*, 2014, **118**, 3844-3852.
32. D. Gerlich, in *State-Selected and State-to-State Ion-Molecule Reaction Dynamics. Part I. Experiment*, eds. C. Y. Ng and M. Baer, John Wiley & Sons, Inc., New York, 1992, vol. 82, pp. 1-176.
33. J. B. Fenn, M. Mann, C. K. Meng, S. F. Wong and C. M. Whitehouse, *Science*, 1989, **246**, 64-71.
34. R. Otto, J. Brox, S. Trippel, M. Stei, T. Best and R. Wester, *Nat. Chem.*, 2012, **4**.
35. F. Liu, R. Emre, W. Lu and J. Liu, *Phys. Chem. Chem. Phys.*, 2013, **15**, 20496-20509.
36. R. A. Marcus, *J. Chem. Phys.*, 1952, **20**, 359-364.
37. L. Sun and W. L. Hase, *Rev. Comput. Chem.*, 2003, **19**, 79-146.
38. A. Midey, I. Dotan and A. A. Viggiano, *J. Phys. Chem. A*, 2008, **112**, 3040-3045.
39. W. J. Lafferty, A. M. Solodov, C. L. Lugez and G. T. Fraser, *Appl. Opt.*, 1998, **37**, 2264-2270.

40. K. M. Ervin and P. B. Armentrout, *J. Chem. Phys.*, 1985, **83**, 166-189.
41. E. D. Lee, W. Muck, J. D. Henion and T. R. Covey, *J. Am. Chem. Soc.*, 1989, **111**, 4600-4604.
42. S. Fürmeier and J. O. Metzger, *J. Am. Chem. Soc.*, 2004, **126**, 14485-14492.
43. D. Fabris, *Mass Spectrom. Rev.*, 2005, **24**, 30-54.
44. G. W. Amarante, M. Benassi, H. M. S. Milagre, A. A. C. Braga, F. Maseras, M. N. Eberlin and F. Coelho, *Chem. Eur. J.*, 2009, **15**, 12460-12469.
45. K. Huvaere, B. Sinnaeve, J. V. Bocxlaer and L. H. Skibsted, *J. Agric. Food Chem.*, 2012, **60**, 9261-9272.
46. L. P. E. Yunker, R. L. Stoddard and J. S. McIndoe, *J. Mass Spectrom.*, 2014, **49**, 1-8.
47. X. Yan, E. Sokol, X. Li, G. Li, S. Xu and R. Graham, *Angewandte Chemie*, 2014, **53**, 5931-5935.
48. F. M. Wampler, A. T. Blades and P. Kebarle, *J. Am. Soc. Mass Spectrom.*, 1993, **4**, 289-295.
49. M. J. Frisch, G. W. Trucks, H. B. Schlegel, G. E. Scuseria, M. A. Robb, J. R. Cheeseman, G. Scalmani, V. Barone, B. Mennucci, G. A. Petersson, H. Nakatsuji, M. Caricato, X. Li, H. P. Hratchian, A. F. Izmaylov, J. Bloino, G. Zheng, J. L. Sonnenberg, M. Hada, M. Ehara, K. Toyota, R. Fukuda, J. Hasegawa, M. Ishida, T. Nakajima, Y. Honda, O. Kitao, H. Nakai, T. Vreven, J. J. A. Montgomery, J. E. Peralta, F. Ogliaro, M. Bearpark, J. J. Heyd, E. Brothers, K. N. Kudin, V. N. Staroverov, T. Keith, R. Kobayashi, J. Normand, K. Raghavachari, A. Rendell, J. C. Burant, S. S. Iyengar, J. Tomasi, M. Cossi, N. Rega, J. M. Millam, M. Klene, J. E. Knox, J. B. Cross, V. Bakken, C. Adamo, J. Jaramillo, R. Gomperts, R. E. Stratmann, O. Yazyev, A. J. Austin, R. Cammi, C. Pomelli, J. W. Ochterski, R. L. Martin, K. Morokuma, V. G. Zakrzewski, G. A. Voth, P. Salvador, J. J. Dannenberg, S. Dapprich, A. D. Daniels, O. Farkas, J. B. Foresman, J. V. Ortiz, J. Cioslowski and D. J. Fox, *Gaussian 09, Rev. B. 01*, (2009) Gaussian, Inc., Wallingford CT.
50. I. M. Alecu, J. Zheng, Y. Zhao and D. G. Truhlar, *J. Chem. Theory Comput.* 2010, **6**, 2872-2887.
51. L. Zhu and W. L. Hase, *A General RRKM Program(QCPE 644), Quantum Chemistry Program Exchange*, (1993) Chemistry Department, University of Indiana, Bloomington.
52. W. L. Hase, K. Bolton, P. de Sainte Claire, R. J. Duchovic, X. Hu, A. Komornicki, G. Li, K. Lim, D. Lu, G. H. Peslherbe, K. Song, K. N. Swamy, S. R. Vande Linde, A. Varandas, H. Wang and R. J. Wolf, *VENUS 99: A general chemical dynamics computer program*, (1999) Texas Tech Univeristy Lubbock, TX.
53. G. H. Peslherbe, H. Wang and W. L. Hase, *Adv. Chem. Phys.*, 1999, **105**, 177-201.
54. V. Bakken, J. M. Millam and H. B. Schlegel, *J. Chem. Phys.*, 1999, **111**, 8773-8777.
55. L. Laaksonen, *gOpenMol*, (2005) Center for Scientific Computing, Espoo, Finland.
56. B. Kovacvić, M. Rožman, L. Klasinc, D. Srzić, Z. B. Maksić and M. Yáñez, *J. Phys. Chem. A*, 2005, **109**, 8329-8335.
57. C. Bleiholder, S. Suhai and B. Paizs, *J Am Soc Mass Spectrom*, 2006, **17**, 1275-1281.
58. T. C. Dinadayalane, G. N. Sastry and J. Leszczynski, *Int. J. Quantum Chem.*, 2006, **106**, 2920-2933.
59. Z. Huang, Z. Lin and C. Song, *J. Phys. Chem. A*, 2007, **111**, 4340-4352.
60. A. K. Y. Lam, C. A. Hutton and R. A. J. O'Hair, *Rapid Comm. Mass Spectrom.*, 2010, **24**, 2591-2604.
61. M. Citir, C. S. Hinton, J. Oomens, J. D. Steill and P. B. Armentrout, *Int. J. Mass Spectrom.*, 2012, **330-332**, 6-15.
62. V. Riffet and G. Bouchoux, *J. Phys. Chem. A*, 2006, **110**, 7303-7306.
63. S. Gronert, D. C. Simpson and K. M. Conner, *J.Am. Soc. Mass Spectrom.*, 2009, **20**, 2116-2123.
64. K. M. Uddin, P. L. Warburton and R. A. Poirier, *J. Phys. Chem. B*, 2012, **116**, 3220-3234.
65. A. K. Rai, W. Fei, Z. Lu and Z. Lin, *Theor Chem Acc*, 2009, **124**, 37-47.
66. C. M. Jones, M. Bernier, E. Carson, K. E. Colyer, R. Metz, A. Pawlow, E. D. Wischow, I. Webb, E. J. Andriole and J. C. Poutsma, *Int. J. Mass Spectrom.*, 2007, **267**, 54-62.
67. W. Kulik and W. Heerma, *Biomed. Environ. Mass Spectrom.*, 1988, **15**, 419-427.
68. N. N. Dookeran, T. Yalcin and A. G. Harrison, *J Mass Spectrom*, 1996, **31**, 500-508.
69. H. E. Aribi, G. Orlova, A. C. Hopkinson and K. W. M. Siu, *J. Phys. Chem. A*, 2004, **108**, 3844-3853.
70. H. Lioe and R. A. J. O'Hair, *Anal. Bioanal. Chem.*, 2007, **389**, 1429-1437.
71. J. M. Matxain, M. Ristilae, A. Strid and L. A. Eriksson, *Chem. Eur. J.*, 2007, **13**, 4636-4642.
72. M. T. Rodgers, K. M. Ervin and P. B. Armentrout, *J. Chem. Phys.*, 1997, **106**, 4499-4508.
73. L. Zhu and W. L. Hase, *Chem. Phys. Lett.*, 1990, **175**, 117-124.
74. K. M. Ervin, I. Anusiewicz, P. Skurski, J. Simons and W. C. Lineberger, *J. Phys. Chem. A*, 2003, **107**, 8521-8529.
75. A. A. Viggiano, A. Midey, N. Eyet, V. M. Bierbaum and J. Troe, *J. Chem. Phys.*, 2009, **131**, 094303.
76. K. B. Wiberg, *Tetrahedron*, 1968, **24**, 1083-1096.

77. A. E. Reed, L. A. Curtiss and F. Weinhold, *Chem. Rev.*, 1988, **88**, 899-926.
78. E. Skovsen, J. W. Snyder, J. D. C. Lambert and P. R. Ogilby, *J. Phys. Chem. B*, 2005, **109**, 8570-8573.
79. C. J. Calleman and V. Poirier, *Acta Chemica Scandinavica B*, 1983, **37**, 809-815.
80. S. Jain, A. Kushwah, P. K. Paliwal and G. N. Babu, *Int. J. Chem. Sci.*, 2010, **8**, 763-768.
81. J. Cadet, T. Douki and J.-L. Ravanat, *Acc. Chem. Res.*, 2008, **41**, 1075-1083.

TOC